Open Research Online

The Open University's repository of research publications and other research outputs

Experimental and numerical study of strength mismatch in cross-weld tensile testing

Journal Item

For guidance on citations see FAQs.

oro.open.ac.uk

Experimental and numerical study of strength mismatch in cross-weld tensile testing

Murat O. Acar[1,2] and Salih Gungor[1]

ABSTRACT

The mechanical properties of welded boiler tubes used in power plants can be significantly altered as a result of the fabrication history, such as pre-straining and heat treatment. The primary aim of the study was to determine the effect of fabrication history on local tensile properties across the welds. This was achieved by testing cross-weld specimens machined from welded thin-walled tubes (with unstrained or pre-strained base metal) before and after heat treatment. Digital image correlation (DIC), which is a full-field strain measurement technique, was implemented in order to obtain the local stress-strain curves and to extract the corresponding local tensile properties such as offset proof stress. Evidence of strain hardening due to the constraint and thermo-mechanical cycles during the welding process was found in the heat-affected-zone (HAZ) and evidence of softening was observed in the pre-strained base metal. It was found that the heat treatment process removed the effect of pre-straining and welding on the proof stress and the strength along the specimen was nearly homogenized. However, mapping the local stress-strain curves in the as-welded cross-weld specimens with pre-strained base metal has revealed abnormal strain-relaxation with increase in load in the weld-affected region. For a better understanding of this behaviour, a tensile test of a cross-weld specimen with a large strength mismatch between the weld metal and the base metal was simulated using the finite element method. It was found that the strength mismatch in the specimen causes the development of bi-axial stresses in the HAZ once local yielding begins and the use of global axial stress to construct the local stress-strain

[1] Department of Engineering and Innovation, Faculty of Mathematics, Computing and Technology, Open University, Walton Hall, Milton Keynes, MK7 6AA, UK.
Corresponding author: salih.gungor@open.ac.uk
[2] Siemens Demag Delaval Turbomachinery, Inc., 840 Nottingham Way, Trenton, NJ 08638, USA.

curve results in an apparent "reduced-strain" anomaly. Nevertheless, for the strength mismatch ratios studied, this anomalous behaviour did not seem to significantly affect the determination of the local proof stress in the specimens.

Keywords: cross-weld tensile testing, strength mismatch, local deformation, digital image correlation, finite element analysis

Introduction

The structural integrity, performance and life of austenitic stainless steel weldments in power generation plants is largely determined by the mechanical properties of the weld metal, the heat affected zone (HAZ) and the base metal. These properties depend on the full fabrication history including cold bending and swaging, welding, heat treatment and the effects of service ageing. For example, many metres of austenitic stainless steel tubes are bent, swaged, welded and heat treated to produce heat exchanger units in the installation of steam raising power plants. Prior to the instalment the mechanical properties of the virgin tube have been greatly altered during manufacturing steps.

The tube-shaping operations such as bending and swaging accumulate plastic deformation in the stainless steel. The plastic deformation can improve the strength of austenitic stainless steels, but it increases the material's susceptibility to stress corrosion and creep damage [1, 2]. For this reason, ASME Boiler and Pressure Vessel Design code [3] specifies forming strain limits for stainless steels for high temperature applications. For example, for 316H type stainless steel the forming limit is 20% strain, if the material is to operate between 580°C and 675°C. If it exceeds that threshold, the material should be annealed above 1040°C to restore its mechanical properties to the start of life values. In addition to the tube shaping, heat exchanger units require welding to produce tube junctions

2

where the main tube with a larger diameter is connected to a U-bent tube. However, very little is known about the effects of welding onto plastically deformed tubes. The effect of heat during welding can alter the material properties around the weld bay either softening or hardening. In case of welding onto bent or swaged tubes, if the temperature is high enough, annealing occurs and this softens the previously work-hardened material. Current construction practices for 316H tubes forbid welding onto material that has experienced more than 15% plastic strain, without first resolution heat treating the material [4]. If the base metal near the weld has a relatively lower yield strength, then the thermal cycles during welding can cause strain hardening or considerable amount of plastic strain near the weld fusion zone [5]. As a result of hardening or softening the material properties change in weld-near regions and this causes a strength variation in the heat affected region. Furthermore, the tube-shaping and welding processes can produce significant level of residual stresses, which can cause premature failures during operation [6]. Therefore, a post weld heat treatment (PWHT) is recommended to relieve the weld residual stresses. However, in practice it is not always possible to follow these codes strictly, especially when the whole boiler is constructed as a single unit and it is then too large and too complex, and possibly contains different tubing materials, to have PWHT applied.

The knowledge of local strength variation in the weld-affected regions is crucial in the structural integrity assessments of these units [7, 8]. Several methods for capturing the spatial variation in tensile properties in weldments have been reported in literature. One such method involves testing of miniature-specimens extracted from different regions of weldments [9–11]. However, the spatial resolution and accuracy that can be achieved using miniature-specimens are limited by the ability to isolate the individual weld regions. Another method is based on the instrumented ball indentation technique [12, 13]. Although the

3

resolution obtainable by the ball indentation method is much better than that can be achieved by miniature-specimens, the technique requires semi-empirical formulas and the conditions generated by multi-axial compression loading are assumed to correlate well with those of uniaxial compression and tension loading. A more promising method involves testing tensile specimens that are machined from weldments to contain the main parts of the weldment within their gauge length (so-called cross-weld specimens) and mapping full field strain at the gauge section using a full-field optical technique [5, 14]. The main advantage of this method over the other methods is that it provides local stress strain curves, from which the variation of mechanical properties such as proof stress across the weldment can be determined.

A common optical method used for these measurements is digital image correlation (DIC), which is based on computational tracking of contrasting surface features (*speckle patterns*) on digital images of the specimen's gauge section taken during deformation. The algorithm used in the DIC technique divides the images into sub-regions and, provided that each sub-region or "subset" has a unique traceable intensity pattern within the immediate vicinity, the algorithm cross-correlates the subset patterns in successive images. It then calculates the relative displacement vector of each subset in each pixel with sub-pixel accuracy [15]. This spatially resolved displacement/strain measurement with DIC enables the investigation of the local material properties in heterogeneous materials, such as welded components. It has been used by several researchers to determine the local material properties of friction stir weldments [14, 16–24], arc weldments [10, 11, 25–29] and laser beam weldments [30, 31] during tensile testing.

In the present study, as part of a project investigating the effect of fabrication history on 316H tube weldments, the local tensile properties of the weldments after different

4

manufacturing steps (pre-straining, welding and heat treatment) have been studied by carrying out tension tests on specimens that were cut perpendicular to the weld line, such that the gauge length of the specimen contained the fusion zone and the heat affected zone (*cross-weld* specimens). The offset proof strength variation across the weldment was obtained on cross-weld tensile specimens from the local stress-strain curves which were constructed using the local displacement measurements by DIC and the global load measured by the load cell unit of the tensile test machine. An anomaly in the form of apparent strain relaxation with increasing applied load was observed in the local stress-strain curves obtained in the HAZ of the cross-welds tensile specimens cut from the tubes that were pre-strained before welding. Similar observations have been reported in literature [21, 25, 29], which were attributed to the use of global stress in calculations and the strength mismatch between the weld and base metals. The global stress is determined directly from the load cell readings of the testing machine and hence the stress is assumed to be uniform throughout the gauge section of specimens ("iso-stress assumption") [14]. Lockwood and Reynolds [17] experimentally and numerically studied the validity of the iso-stress assumption and the level of constraint due to the specimen geometry. They reported that, although the use of global stress was a convenient way of extracting the local material properties, the constraint due to the thickness of the specimen has an influence on the deformation behaviour, which leads to the breakdown of the iso-stress assumption. A numerical modelling work using finite elements has been undertaken in the present study to verify the measured local stress-strain curves by investigating (1) the strength mismatch effect, (2) the influence of strain calculation method and (3) the use of global load in characterising local stress-strain curves. The effect of these anomalies in the prediction of offset proof strength variation across the weld from the local stress-strain curves was also investigated using the finite element simulations.

5

Experimental Procedure

1. Materials

A set of plastically-strained and butt-welded tubes were supplied for the experimental programme by EDF Energy (Table 1). The untreated tubes (referred to as the tubes before plastic straining and welding) were manufactured by extrusion and then solution annealed at 1100°C for 3 minutes followed by water quenching. The final austenite grain size is about 25μm. The tubing material is AISI Type 316H austenitic stainless steel with the composition given in Table 2. The initial tubing geometry was 38 mm in outer diameter and 4 mm in wall thickness. The test specimens were fabricated as follows;

(1) two 450 mm long tubes were pulled uniaxially in tension to give a plastic strain of 10% in the first tube and 20% in the second tube. The pre-straining processes were done using a strain rate of ~0.15%/s with a servo-hydraulic rig. The tube ends were connected to the servo-hydraulic rig using specifically manufactured adaptors, which were welded to the ends of the tubes so that they could be easily fitted to a pair of universal joints for gripping. 25 mm of the tube ends where the adaptors were welded were chopped off after the completion of pre-straining process. The strain during the processing was monitored by a side-mounted extensometer, four strain gauges fitted at 90° intervals around the circumference of the centre of the pipe and by fiducial markings on the pipe length.

(2) The strained tubes and a non-strained tube were cut into two halves.

(3) Following a root tack welding, the matching half-tubes were clamped together and then welded using a tungsten inert gas (TIG) welding process (complying to the welding standard ISO 15614-1) with type 316L filler metal code (Tables 2 and 3). The weld contains two passes: root pass and cap pass. During the root pass the tacks were incorporated into the weld.

A micrograph of the weld cross section and the weld geometry are shown in Fig. 1. A microstructural examination revealed that the weld microstructure is mainly austenite with about 5% delta-ferrite.

Flat tensile test specimens from both the welded part of the tube (*cross-weld* specimens) and the tube ends that were not affected by the welding process (*plain* specimens) were cut using electro-discharge machining (EDM) as shown in Fig. 2. The specimens were then ground flat to a thickness of 3 mm. Standardized tensile test specimens are generally designed according to ASTM E 8/E 8M – 11: Standard Test Methods for Tension Testing of Metallic Materials [32]. However, the dimensions of the specimens have been modified in this work due to the tube geometry. In addition, the gauge length of the *cross-weld* specimens has been designed longer in order to fit all the weld affected zones (the weld metal, the HAZ and the base metal). The actual test specimens with modified dimensions have been machined after the verification tests with dummy samples following FEA simulations to check the stress distribution through the test specimen during tensile test. The cut position and the dimensions of the tensile specimens are given in Fig. 2. The tubes, cross-weld and plain tensile specimens are labelled as shown in Table 1. Some of the specimens were labelled as "HT" to show that they were heat treated at a soaking temperature of 1050°C for 15 minutes under vacuum and quenched to 50°C with nitrogen gas.

2. Tensile testing

Tension tests of plain and cross-weld specimens (B_0, B_{10}, B_{20}, $B_{0\text{-HT}}$, $B_{10\text{-HT}}$, $B_{20\text{-HT}}$ and C_0, C_{10}, C_{20}, $C_{0\text{-HT}}$, $C_{10\text{-HT}}$, $C_{20\text{-HT}}$) were carried out using a screw-driven tensile testing machine with a 30kN load cell. Mechanical wedge action grips were used to fix the specimens into the machine. In addition to DIC measurements, a clip gauge (Instron, 25mm

7

gauge length) was attached to the specimens to measure the extension of the gauge length. Before each test commenced, the loading and specimen alignment was checked using a laser line alignment tool in order to avoid subjecting the specimen to any bending or torsion, i.e. to ensure the loading was purely uniaxial tension [33, 34]. Two universal joints were used to improve axial alignment. Additionally, 2 mm thin aluminium guide plates were placed in the wedge grips to centrally position the shoulders of the specimens with the loading axis of the testing machine.

3. Digital image correlation

The full field distribution of strain was obtained throughout DIC integrated tensile tests of plain and cross-weld specimens. The surface pattern required for the DIC measurements is usually obtained by applying a spray paint. However, in this study, it was found that the speckle pattern obtained by white light illumination of the rough surface produced by EDM gave finer and more consistent speckle pattern, and hence better image correlation [27]. A DC fibre optic light source was used to illuminate the surface. The tensile tests were performed under displacement control with a constant extension rate of 0.1mm/min. During the tests, images of the front surface of the specimens were captured by a digital single lens reflex (DSLR) camera (Nikon D300), with a sensor size of 4,288 x 2,848 pixels, and a 200 mm macro lens. The pixel size for the magnification used corresponded to about 11 μm. The images were taken every 10 seconds and the load and extension from the testing machine were recorded every second. The analysis of the images was performed using a commercial DIC software package [35].

In-plane displacement vectors in the loading direction were calculated within the user-defined working space using a '256×256 subset size with 50% overlap and 2 passes'

and a '128×128 subset size with 50% overlap and 6 passes' respectively. After the displacement map in the loading direction was obtained using the DIC software, the strain was calculated by differentiating the displacement in a user-defined gauge length using a Matlab script. Stress-strain curves were constructed with the averaged strain data for each row and the global stress (i.e. the iso-stress assumption) calculated using the data from the load cell, as shown in Fig. 3. A linear line is fit to the data points in a user-defined range within the elastic regime. This linear line is offset to a required value (0.2%, 1.0%, 2.0% etc) and the proof stress at the input value is taken as the stress component of the point where the offset line and the stress-strain curve intersect.

Experimental Results

1. Plain specimens

Plain tensile test specimens (B_0, B_{10}, B_{20}, B_{0-HT}, B_{10-HT}, B_{20-HT}) were extracted from positions remote from the influence of the welds. Their global tensile stress-strain behaviour is shown in Fig. 4(a). Although they have homogenous material properties, the DIC technique was employed to measure strain in the gauge section of the specimens and compared to those obtained by the extensometer in order to verify the confidence in DIC technique. As can be seen in Fig. 4(b), the results from the extensometer and the DIC measurements show a good correlation for all the specimens. Fig. 4(b) also gives a tabulation of 0.2% and 1% proof stresses derived from these curves.

2. Cross-weld specimens

Cross-weld tensile test specimens (C_0, C_{10}, C_{20}, C_{0-HT}, C_{10-HT}, C_{20-HT}) were extracted across the weldment; therefore, the material properties vary along the gauge length which includes the weld metal, the HAZ and the unaffected base metal (Fig. 4(a)). Hardness

profiles across the weld for the as-welded and heat-treated cross-weld specimens have been obtained using an automated hardness test machine with a load of 5kgf. It can be seen in Fig. 5 that the hardness values in the unaffected base metal are almost constant, but they vary in the weld pool and the HAZ.

Four Kyowa KFG-1-120-C1-16 type strain gauges (SGs), which were 1.1 mm wide and 1 mm long, were glued on the tensile specimens as shown in Fig. 6. The two SGs, which were attached 20 mm away from the weld centre line (WCL) on opposite faces of the specimen, were used to check the alignment of the test fixture. The other two SGs were located on the back surface of the specimen; one SG was glued at the middle of the weld and the other was in the HAZ region (~6.5 mm away from WCL). The local stress-strain curves constructed with the strain data obtained from these latter two SGs were compared to the stress-strain curves constructed with strain data obtained using the DIC measurements for verification. Note that the global stress (iso-stress), which was calculated from the load (kN) recorded from the load cell attached to the crosshead of the Instron testing machine, was used to construct both sets of stress-strain curves.

The full field displacement data obtained by the DIC measurements were used to construct stress-strain curves at every subset (~ 0.5 mm^2) of the test area shown in Fig. 6. These were then used to map the variation of proof stress across the weldment. The complete stress-strain curves at three critical locations are mentioned below.

Local stress-strain curves obtained at the weld centre

Stress-strain curves, which were constructed with the strain data from SGs and DIC at the weld centre, are given in Fig. 7. Results from the two measurement techniques show a good overall correlation, although there are some discernible differences, which may possibly be attributed to the fact that these measurements were made on the opposite sides of

the test specimen. Stress-strain curves obtained from specimens C_0, C_{10} and C_{20} at the weld centre, which represent the weld metal tensile behaviour prior to the heat treatment, are very similar. The tensile behaviour of the weld metal after the heat treatment is depicted in the stress-strain curves obtained from specimens C_{0-HT}, C_{10-HT} and C_{20-HT} at the weld centre. The effect of heat treatment on the weld metal can be clearly seen: 0.2% proof stress of the weld metal prior to heat treatment is between 265-275 MPa, which decreases to about 200-220 MPa after the heat treatment.

Local stress-strain curves obtained at a distance of 6.5mm from the WCL

Stress-strain curves, which were constructed with the strain data from SGs and DIC at the position of 6.5mm from the WCL, are given in Fig. 8. Results from the two measurement techniques show a good correlation for all specimens. (Note that the stress-strain curves obtained from the SG on specimens C_0 and C_{10} end at 2.7% and 0.8% strain, respectively, because the SGs detached unexpectedly during testing). However, there is anomalous behaviour in the curve for the specimen C_{20}; there is an apparent strain relaxation starting at around 200 MPa. This strain relaxation seems to coincide with the start of the strain-hardening that the weld metal experiences after yielding at ~210MPa. This anomaly was also observed in other regions of the HAZ as discussed below.

Local stress-strain curves obtained at a distance of 10mm from the WCL

At 10mm from the WCL in cross-weld specimens, strain data was only obtained from DIC measurements (Fig. 9). The stress-strain curves for the heat-treated specimens C_{0-HT}, C_{10-HT} and C_{20-HT} are very similar to those observed at 6.5mm. Similar to the anomaly detected in specimen C_{20} at 6.5 mm, but somewhat more pronounced here, an apparent strain relaxation effect has been observed for specimens C_{10} and C_{20}. Although this apparent strain relaxation seems to be starting at around 340 MPa for both specimens (the dashed rectangle

in Fig. 9), the change in slope of the elastic line with increasing stress (which will be referred as "reduced-strain" trend hereafter) starts at a lower stress, coinciding with the strain hardening in the weld metal after yielding at ~210MPa. This suggests that, once local yielding starts, the load partitioning is not homogenous throughout the weldment and, hence, the iso-stress assumption that was used to plot the stress-strain curves is no longer valid.

Local stress-strain curves obtained at a distance of 20mm from the WCL

Stress-strain curves obtained from SG and DIC measurements at 20mm from the WCL are given in Fig. 10. It can be seen that C_{10} and C_{20} specimens show a similar anomaly as in the case of 10mm, albeit less pronounced. At 20mm from the WCL the stress-strain curve of C_{10} has both elastic and plastic regions, however, C_{20} is still in the elastic region and does not reach yielding point when the failure occurs in the weld metal. The stress-strain curve of C_{10} is very similar to that of plain specimen, B_{10} (Fig. 4(b)), which suggests that beyond 20 mm from the WCL, there is no effect of welding on mechanical properties. The heat-treated specimens C_{0-HT}, C_{10-HT} and C_{20-HT} show again a similar stress-strain behaviour as in Figures 8 and 9.

The stress-strain curves obtained from the base metal and the HAZ at different positions suggest that the welding and heat treatment has a considerable influence on the material properties of the unstrained and pre-strained base metal. It was observed that the pre-strained base metal becomes softer closer to the fusion boundary after welding. As mentioned above, some of the stress-strain curves obtained from the pre-strained base metal in non-heat-treated condition showed some anomalies. The unstrained base metal was also affected by the welding process; the hardness and the strength of both the weld and the base metal were lower after the heat treatment. Stress-strain curves obtained from the heat-treated

specimens (C_{0-HT}, C_{10-HT} and C_{20-HT}) at different positions in the base metal suggest that the mechanical properties are very similar at these positions.

For a better understanding of the variation in material properties, the proof stress distribution is given in Fig. 11 which plots the variation of 0.2% proof stress on one side of the WCL for the cross-weld specimens based on the analysis of the DIC stress-strain curves. In specimen C_0, the proof stress increases from a minimum of 268 MPa in the weld region to a maximum of 319 MPa at about 10mm from the WCL and then drops gradually to a steady value of 285 MPa at about 25mm from the WCL. In specimen C_{10}, the proof stress increases steadily from a minimum of 260 MPa in the weld region to a maximum of about 565 MPa at 16mm from the WCL, where it levels off. The trend in proof stress for specimen C_{20} is similar to C_{10} but in this case the material beyond 8.5mm did not show any yielding (since fracture already took place in the softer weld metal before the yield stress level of the material beyond 8.5mm was reached) and hence the proof stress could not be derived. In specimen C_{0-HT}, the proof stress increases from a minimum of 200 MPa in the weld region to a maximum of about 250 MPa at 7mm from the WCL and it remains almost constant beyond that point. In specimens C_{10-HT} and C_{20-HT}, the trend in proof stress distribution is quite similar. Apart from a small increase just after the weld interface, the specimens C_{0-HT}, C_{10-HT} and C_{20-HT} show almost identical yielding behaviour. The proof stresses obtained from SGs are tabulated in Fig. 11. Results from the DIC and the SGs show a good correlation in general. However, the proof stress obtained from the SG on specimen C_0 at WCL is 290 MPa whereas the DIC gives 275 MPa. Note that the SGs are on the opposite half and at the back surface of the specimen. Proof stresses obtained from the back and front SGs at 20mm away from the WCL for specimens C_0 and C_{10} are very similar, which confirms the alignment of the loading fixture and the specimen was correct.

13

FE validation of DIC integrated tension test of a cross-weld specimen with strength mismatch

The hardness profile in Fig. 5 suggests that specimens C_0, $C_{0\text{-HT}}$, $C_{10\text{-HT}}$ and $C_{20\text{-HT}}$ are almost homogenous whereas the non-heat-treated base metal of the specimens C_{10} and C_{20} are much stronger than the weld metal, which means that there is a strength mismatch in those specimens.

During tensile testing of a cross-weld specimen with a significant strength mismatch level, as in the case of the specimens C_{10} and C_{20}, the strong metal can constrain the plastic deformation of the soft metal and bi-axial stresses can develop during yielding at the interface they join. Therefore, these bi-axial stresses can influence the yielding behaviour of the material in the vicinity. So, the softer material may start to deform at a higher applied stress than those observed in homogeneous materials and this may affect the local stress-strain curves which are constructed using the uniaxial stress and strain information.

In order to understand the effect of strength mismatch on cross-weld specimens and validate the experimental results, a finite element model was developed. The main aims were to investigate: (1) the constraint effects in under-matched strength condition ($\sigma_{y\text{-base}} > \sigma_{y\text{-weld}}$), (2) the effect of the strain computation technique on the apparent stress-strain curves and (3) the validity of the iso-stress assumption. The results were also expected to provide information on the reliability of the prediction of offset proof strength variation across the weld from the local stress-strain curves showing the anomalies in the elastic region of sections with higher proof strength.

1. Finite Element Model

A 2D multi-material model with plane stress elements was developed with the assumption that the weld geometry was symmetrical through the thickness of the specimens.

14

The 2D plane stress assumption was also used by Lockwood and Reynolds, who have found that plane stress model gives very comparable results with DIC measurements in thin (2.7mm) tensile specimens [17]. In specimens C_{10} and C_{20} there is a gradually softened zone (i.e. HAZ) where the local yield strength increases continuously from the weld boundary to the unaffected base metal. Therefore, the yield strength in the model was assumed to increase linearly from the weld metal to the unaffected base metal as shown in Fig. 12. The strength mismatch level is given as the ratio of the yield stress of the weld and the base metals. Therefore, for this model the strength mismatch level was selected as 0.3. The size of each zone was estimated by using the hardness map of the specimens C_{10} and C_{20}.

Because of its simplicity, modelling a partitioned HAZ region in cross weld tension specimens has been very common [17, 20, 36]. However, varying the material properties between the weld and the unaffected base metal in a stepwise manner creates an artificial interface between each HAZ partition which results in unrealistic biaxial stress state at each interface. In the multi-material model used in this study, a continuous HAZ material in which the properties are functionally graded was generated by the ABAQUS user-subroutines [37].

This finite element model, which had 1518 elements and 4853 nodes (Fig. 13), was analysed using ABAQUS Version 6.7 [37]. Quadrilateral CPS8R (reduced integration, eight-node element) type plane stress elements were used in the models. The boundary conditions were selected to simulate the actual tension tests of cross-weld specimens; i.e. the bottom end of the specimen was fixed and the top end was pulled with a constant displacement rate of 0.1mm/min. The FE analysis was static and non-linear, based on isotropic elastic–plastic materials with isotropic work-hardening. Strain rate dependency was not taken into account since the displacement rate was small.

2. Numerical Results

<u>Local stress-strain curves</u>

In order to investigate whether the anomalies observed in tension tests were caused by a real material behaviour or were a result of experimental inadequacies, such as the use of iso-stress assumption, local true-stress versus true-strain curves obtained by the FE modelling were examined. The effect of strain averaging along the width and the use of global stress on the shape of a local stress strain curve in HAZ are demonstrated in Fig. 14, where four different stress-strain curves are plotted to show the local deformation behaviour at 7.75mm away from the WCL. These curves are compared to the input stress-strain curve (see −✳−) in the same figure. Note that the stress and the strain used to construct these curves are in the loading direction as it was measured during the DIC integrated tension tests. These four stress-strain curves are:

(1) "stress @ mid-width" vs. "strain @ mid-width" curve (see −△− on Fig. 14) which was constructed by the axial stress and axial strain calculated for the middle domain (filled domain in Fig. 14) at 7.75mm from the WCL. This curve represents the original local deformation behaviour in this domain when the whole specimen is under tension.

(2) "averaged-width stress" vs. "averaged-width strain" curve (see −⊟− on Fig. 14) which was constructed by the axial stress and strain, both averaged along the full-width (all unfilled domains + the filled domain in the middle) at 7.75mm from the WCL. This curve represents the original local deformation behaviour averaged over the domains lying along the width at a distance of 7.75mm from the WCL.

(3) "global stress" vs. "strain @ mid-width" curve (see −▲− on Fig. 14). The curve (1) was modified by using the global stress (iso-stress) instead of the "stress @ mid-width" because the experimental local-stress-strain curves can only be constructed

16

using the global stress as the local stress cannot be measured. Therefore, this curve represents one of the extremes for the experimental way of constructing the local stress-strain curve using local strain at a point and the global stress. This enables the spatially-resolved local deformation behaviour on the sample surface to be obtained, as it was used by Reynolds and Duvall [14].

(4) "global stress" vs. "averaged-width strain" curve (see —■— on Fig. 14). The curve (2) was modified by using the global stress instead of the "averaged-width stress" due to not being able to measure local stress. This curve represents another extreme for the experimental way of constructing the local stress-strain curve using the averaged-strain along the width at a specific distance from the WCL and the global stress.

Iso-stress assumption (the use of global stress) in DIC analyses means that the stress, which is used to construct the local stress-strain curves, is uniform along the specimen gauge length and is calculated by dividing the global load to the original cross-section of the specimen. In FE analyses, the stress averaged across the width at 24.5mm away from the WCL was considered as the "global stress", since at 24.5mm away from WCL and further away towards the end of the specimen the axial stress is uniform across the width and there is very small deformation in the transverse direction during the simulation.

In Fig. 14, it can be seen that there is no anomaly on curves (1) and (2), although they are different from the input stress-strain curve. The use of global stress instead of "averaged-width stress" does not influence the stress-strain behaviour (see curves (2) and (4)). On the other hand, the use of global stress instead of "stress @ mid-width" considerably modifies the stress-strain behaviour (see curves (1) and (3)). On curve (3), the most significant modification is the "reduced-strain" trend, i.e., the change in the slope of the elastic region

17

after 250MPa. This "reduced-strain" trend on curve (3) was observed in the experimental local stress-strain curves at 10mm (in the HAZ) from the WCL for specimens C_{10} and C_{20} (Fig. 9). Note that curve (3) employs "strain @ mid-width" whereas the experimental local stress-strain curves employ averaged-width strain. This conflict briefly happens because of the definition of the working space in which the displacement vectors were calculated. The working space was defined as a rectangular area which does not include whole of the specimen width (includes only 3.5mm in the middle of a 6mm specimen width) because, for practical reasons, the working space selected is based on the last image where the specimen has shrunk considerably due to Poisson effect.

Reliability of the proof stress distribution

It was shown in Fig. 14 that the use of global stress and strain-averaging across the width of the specimen influences the local stress-strain curves. Experimentally, local stress-strain curves which were constructed with global stress and strain averaging across the width were used to predict the 0.2% offset proof stress along the half the length of the cross-weld specimens (see Fig. 11). In order to check the reliability of the experimental prediction of the proof stress distribution in a cross-weld specimen with strength mismatch, the numerical local stress-strain curves, which were constructed with FE results by using the same experimental assumptions, were employed to predict the 0.2% and 1% proof stresses. In Fig. 15, 0.2% and 1% proof stress determined from the input stress-strain curves is compared with the proof stress distributions predicted from two types of local stress-strain curves; curve (3), which was obtained by plotting "global stress" vs. "strain @ mid-width", and curve (4), which was obtained by plotting "global stress" vs. "averaged-width strain". It can be seen that although the DIC experimental procedure and strength mismatch has affected the local stress-strain curves, the use of curve (3) on the determination of the 0.2% and 1% proof stress

18

distributions has a negligible effect. In the HAZ region, when compared to the input 0.2% proof stress, curve (3) gives a very similar proof stress (~1MPa higher than the input data), whereas curve (4) gives a considerably lower proof stress (~40MPa lower). Similarly, compared to the input 1% proof stress, curve (3) gives a very similar proof stress (~4MPa higher), whereas curve (4) gives a lower proof stress (~25MPa lower).

Discussion

1. Effects of manufacturing steps on tensile properties

Pre-straining

Pre-straining has a considerable effect on the strength of the base material. The 0.2% proof strength of the plain specimens B_0, B_{10} and B_{20} are 295MPa, 557MPa and 689MPa, respectively (Fig. 4(b)). The increase in the strength is due to the accumulation of plastic strain in the material after pre-straining [38]. The accumulated plastic strain after pre-straining can be qualitatively determined by hardness measurements. The hardness values of the non-strained, 10% pre-strained and 20% pre-strained base material are 154, 218 and 251 H_V, respectively (Fig. 5).

Welding

It was found that the 0.2% proof stress in the weld is between 260-280MPa and is similar for specimens C_0, C_{10} and C_{20}. It was also observed that the hardness values of the weld in all three tubes are the same (150 H_V). The difference in stress-strain curves obtained from SG and DIC (Fig. 7) confirms that the material properties of the front and back surfaces are possibly different since the back surface represents the root pass whereas the front surface represents the cap pass.

19

The slight increase in proof stress (Fig. 11) and hardness (Fig. 5) of specimen C_0, in the base metal between 5 and 25mm from the WCL is associated with hardening during the welding process. The hardening in the base metal near the fusion boundary was reported in the thermo-mechanical welding simulations of the stainless steels [39, 40]. The hardening response of this stainless steel tube during a welding thermo-mechanical cycle is very complicated because of the wide ranges of imposed temperature, total strain and strain rate, and because of the potential recovery, recrystallization, creep and visco-plastic effects at high temperatures [39]. Smith *et al* [39] have developed a numerical model for the accurate prediction of the weld residual stresses in 3-pass groove welds of a 316L stainless steel plate. In their simulation, the material model was based on a thermo-mechanical hardening behaviour which considers the cyclic strain hardening and annealing phenomena. They observed that plastic strain accumulation occurs in the base metal adjacent to the weld bead after each weld thermo-mechanical cycle. Their observation was confirmed by spatially resolved proof stress data on cross-weld samples cut from each weld pass using ESPI (electron speckle pattern interferometry) integrated tension tests [5]. They measured 4-6.5% plastic strain in the heat-affected zones of different cross-weld samples. Similarly, Shan *et al* [40] has developed a 3D thermo-mechanical model of a single-bead-on-plate weld (316L stainless steel) and reported accumulation of 4-8% plastic strain near the weld bead in the base metal due to welding.

The effect of welding onto plastically strained materials in terms of hardness and 0.2% proof stress can be seen in Figures 5 and 11, respectively. There is a marked drop in hardness and proof stress for the pre-strained and welded samples approaching the weld from about 16mm away from the WCL. This is caused by the welding process. Base metal near the weld was heated to temperatures where dislocation annealing mechanisms are known to

20

take place. During welding of tube A_0, it was recorded that the peak temperatures had reached 800°C, 550°C and 400°C at 9, 14 and 19mm away from the WCL, respectively. It is known that the annealing temperature of a metal can be lowered by increasing the amount of cold work [41]. It was observed in this study that the austenite grain size increases with amount of cold work from about 25µm (no plastic strain) to 45µm (20% plastic strain) at 1mm distance from the fusion boundary. These findings suggest that the pre-strained base metal adjacent to weld (about 1-1.5mm from the fusion boundary) was annealed due to the heat produced by welding. The gradual decrease in proof stress towards the fusion boundary may be explained with partial softening (recovery).

Heat Treatment

Heat treatment at 1050°C with a soaking time of 15 minutes has a significant influence on the tensile properties of the plain and the cross-weld specimens. The 0.2% proof strength of the plain specimens decreases dramatically after the heat treatment. The 0.2% proof stress of specimens $B_{0\text{-HT}}$, $B_{10\text{-HT}}$ and $B_{20\text{-HT}}$ are 249, 218 and 225MPa, respectively (Fig. 4(b)).

Surprisingly, the stress-strain curves of the specimens $B_{10\text{-HT}}$ and $B_{20\text{-HT}}$ are below the stress-strain curve of the specimen $B_{0\text{-HT}}$. This can be attributed to the Hall-Petch grain size effect [42, 43]. The micrographs of the plain samples before and after heat treatment are given in Fig. 16. Prior to the heat treatment, the grain size of both non-strained and pre-strained material is ~30µm in the straining direction. However, after the heat treatment the grain size of plain material is almost unchanged at about 28 µm, whereas the grain size of the pre-strained materials was almost doubled (>50 µm), which resulted in lower strength.

It has been found that the heat treatment has also altered the tensile properties of the cross-weld specimens. The proof stress of the weld metal decreased by 60MPa as a result of

21

the heat treatment. This can be attributed to the decrease in ferrite content in the microstructure. Austenitic stainless steel welds usually contain unstable delta ferrite, which is known to prevent hot-cracking during solidification. The AISI 316L weld metal in the samples tested in this work contained about 5% delta-ferrite. However, since delta-ferrite is an unstable phase, it partially transforms to austenite at the heat treatment temperature of 1050°C. Decreasing ferrite content is generally known to result in a decrease in room-temperature strength [30]. The decrease in 0.2% proof stress of the base metal in specimens C_{0-HT}, C_{10-HT} and C_{20-HT} is similar to the decrease in the proof stress of plain specimens B_{0-HT}, B_{10-HT} and B_{20-HT}. The hardness profiles on heat-treated cross-weld samples (Fig. 5) agrees well with the proof stress distribution on cross-welds C_{0-HT}, C_{10-HT} and C_{20-HT} (Fig. 11).

It can be concluded that the effect of pre-straining on mechanical properties has been eradicated by the heat treatment process.

2. Local stress-strain curves

Local strains were measured with DIC and SGs during the tension tests of cross-weld specimens. Since it is not possible to measure local stresses in a composite specimen during the tension test, in the construction of local stress-strain curves, the global stress was used. Anomalies have been observed at around 340 MPa on some of the experimental curves obtained from C_{10} and C_{20} specimens (Fig. 9). A realistic FE model of the cross-weld specimen with strength mismatch was useful to understand why these anomalies exist on some curves, which are discussed below.

In a tension test of a homogenous specimen the stress is purely axial and no stress develops in the transverse or through thickness direction in the gauge length until necking

22

starts. However, in a tension test of a cross-weld specimen, biaxial stresses develop after yielding starts due to the strength mismatch. The strong metal can constrain the deformation of the soft metal and bi-axial stresses can develop at the interface. The development of stresses in the loading and transverse direction during the tension test of a cross-weld specimen with strength mismatch is shown in Fig. 17. According to the 2D von Mises yielding criteria, the development of transverse stresses will affect the yielding behaviour of the metal. The reason why curves (1) and (2) in Fig. 14 are different than the input stress-strain curve is the development of biaxial stresses and strains as demonstrated in Fig. 17.

In Fig. 14, it was observed that, when averaged-width strain was used, the use of global stress instead of actual averaged-width stress does not modify the local stress-strain curve (see curves (2) and (4)). This means that the actual stress averaged across the full-width at 7.75mm is very similar to the global stress. On the other hand, it was found out that when strain at the mid-width at 7.75mm from WCL was used, the use of global stress instead of actual stress at mid-width creates an anomaly as observed experimentally (see curves (1) and (3)). The reason for that is the non-uniform axial stress distribution throughout the specimen as shown in Fig. 17(a), which results in a significant difference between the global stress and the actual axial stress at mid-width at 7.75mm.

Fig. 15 shows that the proof stress prediction using the curve (3) ("global stress" vs. "strain @ mid-width") is more reliable compared to that using curve (4) ("global stress" vs. "averaged-width strain"). It can be seen from Fig. 15(b) that even 1% proof stress prediction using curve (4) is 25MPa less than the input 1% proof stress. The reason why curve (4) does not predict the proof stress well, despite not showing any anomaly, is because it does not represent the input stress-strain curve well. On the other hand, even though there is anomaly

on curve (3) due to the use of global stress, it is similar to the input stress-strain curve (see Fig.14).

The deformation behaviour at mid-width at 7.75mm from WCL is governed by the corresponding local input stress-strain curve. Therefore, curve (3) is expected to be similar to the input stress-strain curve when (i) the global stress is close to the equivalent stress at mid-width and (ii) the axial strain at mid-width is close to the equivalent strain at mid-width. Note that the similarity between the curve (3), or curve (4), and the input stress-strain curve will change depending on the combined effect of the specimen geometry, length of the HAZ and the strength mismatch between the base and weld metals.

Conclusions

It has been shown that the DIC technique can successfully be used to map local strain variations in welded joints during tensile testing. The technique has been employed to study the effect of pre-straining on the properties of welded thin-walled tubes manufactured from AISI 316H type stainless steel.

The tensile tests of the plain specimens cut from the studied tubes showed that the pre-straining the material to 10% and 20% increases the proof stress about 190% and 230%, respectively. The effect of pre-straining, however, could be reversed by applying an appropriate heat treatment procedure. The effect of pre-straining on proof stress was also considerable in cross-weld specimens cut from the welded-tubes. The mapping of the proof stress across the weldment revealed that, although no significant increase in the proof stress was observed within the weld metal, it gradually increased in the HAZ away from the WCL, reaching to the plain metal levels at about 20 mm from the WCL. As in the plain specimens,

the effect of pre-straining disappeared in the cross-weld specimens and the proof stress along the specimens was nearly homogenized after the heat treatment at 1050°C for 15 minutes.

Strength mismatch within the weld affected zone resulted in apparent strain relaxation in local stress-strain curves when strain fields obtained by DIC was constructed using global stress calculated from the applied load. The reason for this is that once local yielding begins in a region with lower yield strength, the surrounding region with higher yield strength constrain the softer material and biaxial stresses develop in the region. FE simulation of a tension test of a cross-weld specimen using a multi-material model confirmed that bi-axial stresses develop progressively within the HAZ between the already plastically deformed region and the adjacent region that hasn't yielded yet. The biaxial stress state changes the local yielding behaviour of the material and hence the use of global axial stress to construct the local stress-strain curve in the HAZ where the bi-axial stresses progressively develop produces an experimental anomaly where the strain appears to relax in the elastic regime with increasing strain. FE modelling results suggest that the use of global stress to calculate the proof stress in the specimens showing the reduced-strain anomaly caused by the strength mismatch level of 0.3 produces less than 8% error in proof stress when strain fields were obtained from the middle section (strain @midwidth) of the cross-weld specimen tests.

References

1. Kamaya M, Wilkinson a, Titchmarsh J (2006) Quantification of plastic strain of stainless steel and nickel alloy by electron backscatter diffraction. Acta Materialia 54:539–548. doi: 10.1016/j.actamat.2005.08.046

2. Willis M, McDonaugh-Smith A, Hales R (1999) Prestrain effects on creep ductility of a 316 stainless steel light forging. International Journal of Pressure Vessels and Piping 76:355–359. doi: http://dx.doi.org/10.1016/S0308-0161(99)00007-1

3. ASME Boiler and Pressure Vessel Code, Section I: Rules for Construction of Power Boilers. ASME, New York, USA

4. Spindler MW (2008) Effects of plastic strain and heat treatment on microstructure and properties of 316 stainless steel tubing (Personal Communication).

5. Turski M, Smith MC, Bouchard PJ, et al. (2009) Spatially Resolved Materials Property Data From a Uniaxial Cross-Weld Tensile Test. Journal of Pressure Vessel Technology 131:1–7. doi: 10.1115/1.4000196

6. Lampman S (1997) Weld Integrity and Performance. ASM International

7. (2009) R6 Revision 4 Assessment of the Integrity of Structures containing Defects. British Energy Generation Limited, Gloucester, UK

8. (2003) R5 Issue 3 Assessment Procedure for High Temperature Response of Structures. British Energy Generation Limited, Gloucester, UK

9. Cam G, Erim S, Yeni C, Kocak M (1999) Determination of Mechanical and Fracture Properties of Laser Beam Welded Steel Joints. Welding Research Supplement 78:193–201.

10. Kartal M, Molak R, Turski M, et al. (2007) Determination of Weld Metal Mechanical Properties Utilising Novel Tensile Testing Methods. Applied Mechanics and Materials 7-8:127–132.

11. Molak R, Paradowski K, Brynk T, et al. (2009) Measurement of mechanical properties in a 316L stainless steel welded joint. International Journal of Pressure Vessels and Piping 86:43–47. doi: 10.1016/j.ijpvp.2008.11.002

12. Malow TR, Koch CC, Miraglia PQ, Murty KL (1998) Compressive mechanical behavior of nanocrystalline Fe investigated with an automated ball indentation technique. Materials Science and Engineering: A 252:36–43. doi: http://dx.doi.org/10.1016/S0921-5093(98)00661-3

13. Haggag FM, Nanstad RK, Hutton JT, et al. (1990) Use of Automated Ball Indentation to Measure Flow Properties and Estimate Fracture Toughness in Metallic Materials. In: Braun AA, Ashbaugh NE, Smith FM (eds) Applications of Automation Technology to Fatigue and Fracture Testing, ASTM 1092. American Society for Testing and Materials, Philadelphia, pp 188–208

14. Reynolds AP, Duvall F (1999) Digital image correlation for determination of weld and base metal constitutive behavior. Welding Research Supplement 78:355–360.

15. Sutton MA, Orteu JJ, Schreier HW (2009) Image Correlation for Shape, Motion and Deformation Measurements- Basic Concepts, Theory and Applications. Image Rochester NY 341. doi: 10.1007/978-0-387-78747-3

16. Lockwood W, Tomaz B, Reynolds A (2002) Mechanical response of friction stir welded AA2024: experiment and modeling. Materials Science and Engineering A 323:348–353. doi: 10.1016/S0921-5093(01)01385-5

17. Lockwood WD, Reynolds AP (2003) Simulation of the global response of a friction stir weld using local constitutive behavior. Materials Science and Engineering A 339:35–42. doi: 10.1016/S0921-5093(02)00116-8

18. Sutton M, Yang B, Reynolds a, Yan J (2004) Banded microstructure in 2024-T351 and 2524-T351 aluminum friction stir weldsPart II. Mechanical characterization. Materials Science and Engineering A 364:66–74. doi: 10.1016/S0921-5093(03)00533-1

19. Liu S, Chao YJ (2005) Determination of global mechanical response of friction stir welded plates using local constitutive properties. Modelling and Simulation in Materials Science and Engineering 13:1–15. doi: 10.1088/0965-0393/13/1/001

20. Genevois C, Deschamps a, Vacher P (2006) Comparative study on local and global mechanical properties of 2024 T351, 2024 T6 and 5251 O friction stir welds. Materials Science and Engineering: A 415:162–170. doi: 10.1016/j.msea.2005.09.032

21. Hatamleh O (2008) Effects of peening on mechanical properties in friction stir welded 2195 aluminum alloy joints. Materials Science and Engineering: A 492:168–176. doi: http://dx.doi.org/10.1016/j.msea.2008.03.017

22. Zadpoor AA, Sinke J, Benedictus R (2008) The effects of friction stir welding on the mechanical properties and microstructure of 7000 series aluminium tailor-welded blanks. International Journal of Material Forming 1:1311–1314. doi: 10.1007/s12289-008-0144-7

23. Brown R, Tang W, Reynolds AP (2009) Multi-pass friction stir welding in alloy 7050-T7451: Effects on weld response variables and on weld properties. Materials Science and Engineering A 513–514:115–121. doi: 10.1016/j.msea.2009.01.041

24. Hatamleh O, Mishra RS, Oliveras O (2009) Peening effects on mechanical properties in friction stir welded AA 2195 at elevated and cryogenic temperatures. Materials Design 30:3165–3173. doi: 10.1016/j.matdes.2008.11.010

25. Sutton MA, Yan JH, Avril S, et al. (2008) Identification of heterogeneous constitutive parameters in a welded specimen: uniform stress and virtual fields methods for material property estimation. Experimental Mechanics 48:451–464.

26. Sierra G, Wattrisse B, Bordreuil C (2008) Structural Analysis of Steel to Aluminum Welded Overlap Joint by Digital Image Correlation. Experimental Mechanics 48:213–223. doi: 10.1007/s11340-007-9112-2

27. Acar M, Gungor S, Ganguly S, et al. (2009) Variation of Mechanical Properties in a Multi-pass Weld Measured Using Digital Image Correlation. Society of Experimental Mechanics (SEM) Annual Conference Proceeding

28. Acar M, Gungor S, Bouchard P, Fitzpatrick ME (2010) Effect of prior cold work on the mechanical properties of weldments. Society of Experimental Mechanics (SEM) Annual Conference Proceeding

29. Adeeb S, Horsley D, Yan J, et al. (2006) Local stress-strain response of an axial X100 girth weld under tensile loading using digital image correlation. Proceedings of IPC

30. Boyce BL, Reu PL, Robino C V (2006) The constitutive behavior of laser welds in 304L stainless steel determined by digital image correlation. Metallurgical and Materials Transactions A 37:2481–2492. doi: 10.1007/BF02586221

31. Robino C V., Boyce BL (2008) Constitutive Properties of Dissimilar Metal Laser Welds. Trends in Welding Research 2008 (ASM International) 610–616.

32. ASTM Standard E8 / E8M -11 (2012) "Standard Test Methods for Tension Testing of Metallic Materials."ASTM International, West Conshohocken ,PA

33. Christ BW, Swanson SR (1976) Alignment problems in the tensile test. Journal of Testing and Evaluation (JTE) 4:405–417.

34. Gray TGF, McCombe A (1992) Influence of specimen dimension and grip in tensile testing steel to EN 10 002. Ironmaking and Steelmaking 19:402–408.

35. DaVis 7.2 Data Acquisition and Visualization Software.

36. Rodrigues DM, Menezes LF, Loureiro A, Fernandes J V (2004) Numerical study of the plastic behaviour in tension of welds in high strength steels. International Journal of Plasticity 20:1–18. doi: 10.1016/S0749-6419(02)00112-2

37. ABAQUS Standard/User's Manual, Version 6.7.

38. Smith DJ (2003) The influence of prior loading on structural integrity. In: Milne I, Ritchie R, Karihaloo B (eds) Comprehensive Structural Integrity. Elsevier, London, pp 288–345

39. Smith MC, Bouchard PJ, Turski M, et al. (2012) Accurate prediction of residual stress in stainless steel welds. Computational Materials Science 54:312–328. doi: 10.1016/j.commatsci.2011.10.024

40. Shan X, Davies CM, Wangsdan T, et al. (2009) Thermo-mechanical modelling of a single-bead-on-plate weld using the finite element method. International Journal of Pressure Vessels and Piping 86:110–121. doi: http://dx.doi.org/10.1016/j.ijpvp.2008.11.005

41. Marshall P (1984) Austenitic Stainless Steels: Microstructure and Mechanical Properties. Elsevier Applied Science Publishers

42. Sylwestrowicz W, Hall EO (1951) The Deformation and Ageing of Mild Steel. Proceedings of the Physical Society Section B 64:495–502. doi: 10.1088/0370-1301/64/6/305

43. Petch NJ (1953) The cleavage strength of polycrystals. J Iron Steel Inst 174:8.

Tables

Table 1 Photographs of the tubes and labelling of the test specimens
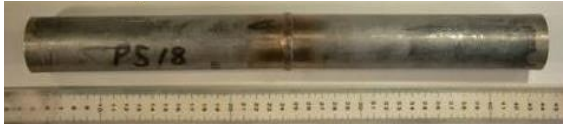
Pre-strained and welded tubes	Degree of plastic deformation	Label of tubes	Label of the plain tensile specimens	Label of the cross-weld tensile specimens
	0%	A_0	B_0, B_{0-HT}	C_0, C_{0-HT}
	10%	A_{10}	B_{10}, B_{10-HT}	C_{10}, C_{10-HT}
	20%	A_{20}	B_{20}, B_{20-HT}	C_{20}, C_{20-HT}

Table 2 Chemical composition of the stainless steel tubing material (Type 316H) and the weld material (Type 316L)

	Cr	Ni	Mo	Mn	Si	Co	C
316H	16.89	11.25	2.04	1.55	0.53	0.089	0.05
316L	18.38	12.07	2.53	1.61	0.37	-	0.01

Figures
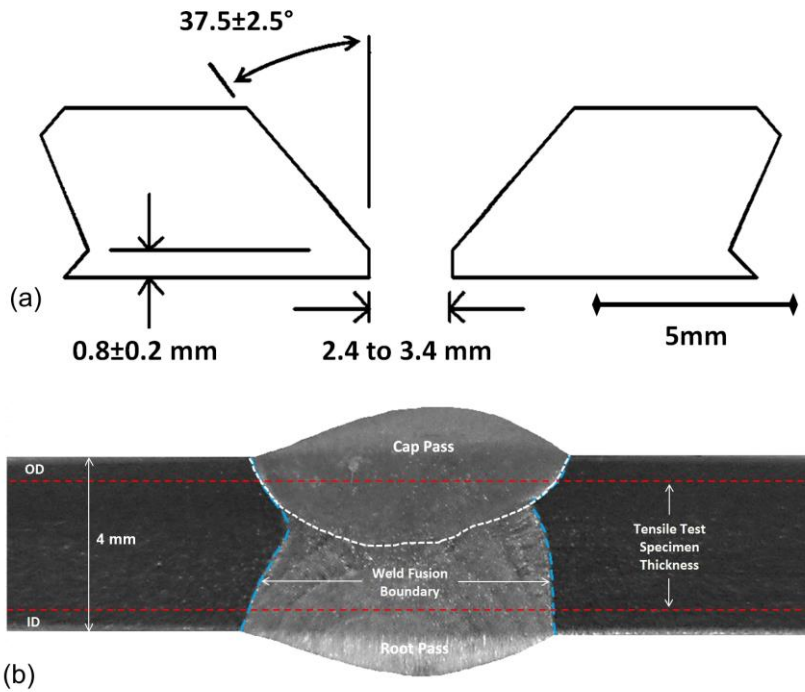
Fig. 1 (a) Weld preparation; (b) Micrograph of the weld cross-section.
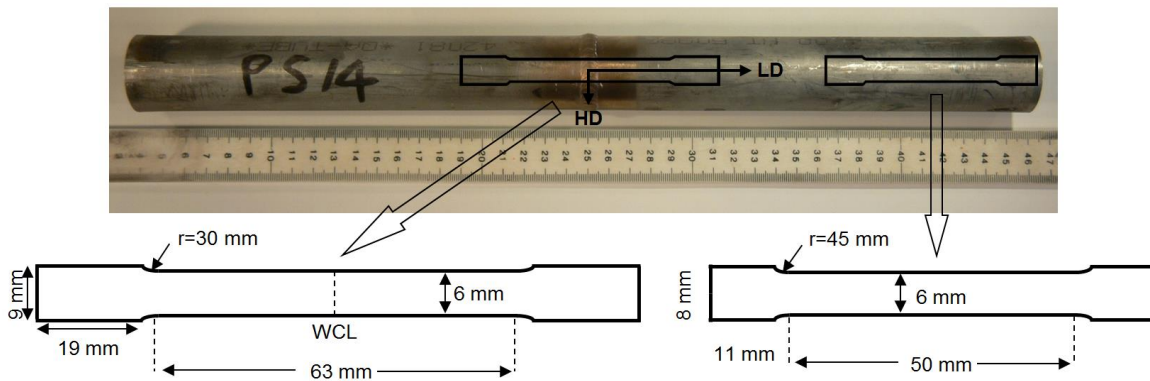
Fig. 2 The cut position (top), and the dimensions of the cross-weld test specimens (bottom left) and plain specimens (bottom right). Both types of specimens are 3mm thick. (LD: longitudinal direction of the tube parallel to the pre-straining direction, HD: hoop direction of the tube perpendicular to the pre-straining direction, RD (into the page): radial direction of the tube perpendicular to the pre-straining direction).

Displacement vectors (Δy) for each subset (n) in the loading direction

$$\varepsilon_n = \frac{(\Delta y_{(n+k)} - \Delta y_{(n-k)})}{(y_{(n+k)} - y_{(n-k)})}$$

Strain computation
$\Delta y_{(n)} \rightarrow$ displacement
$y_{(n)} \rightarrow$ y-coordinate

Strain mapping in the working space

Averaged strain across the row

- Construction of stress-strain curve for each averaged subset
- Linear line fitting to the data points in a user-defined range within the elastic regime
- Determination of 0.2% proof stress
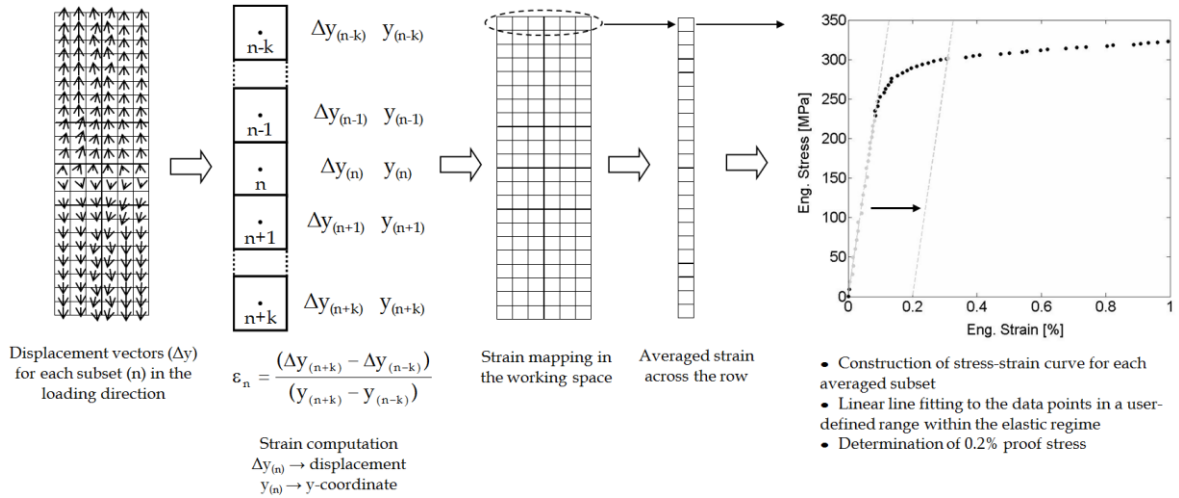
Fig. 3 Flow chart for the determination of the proof stress distribution from DIC displacement measurements with Matlab scripts.
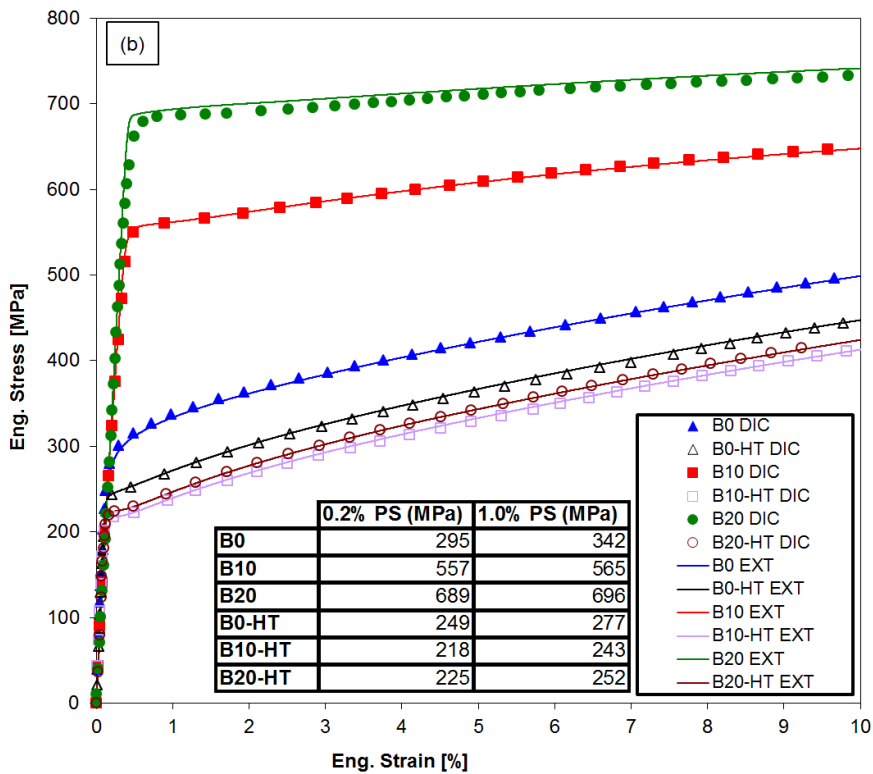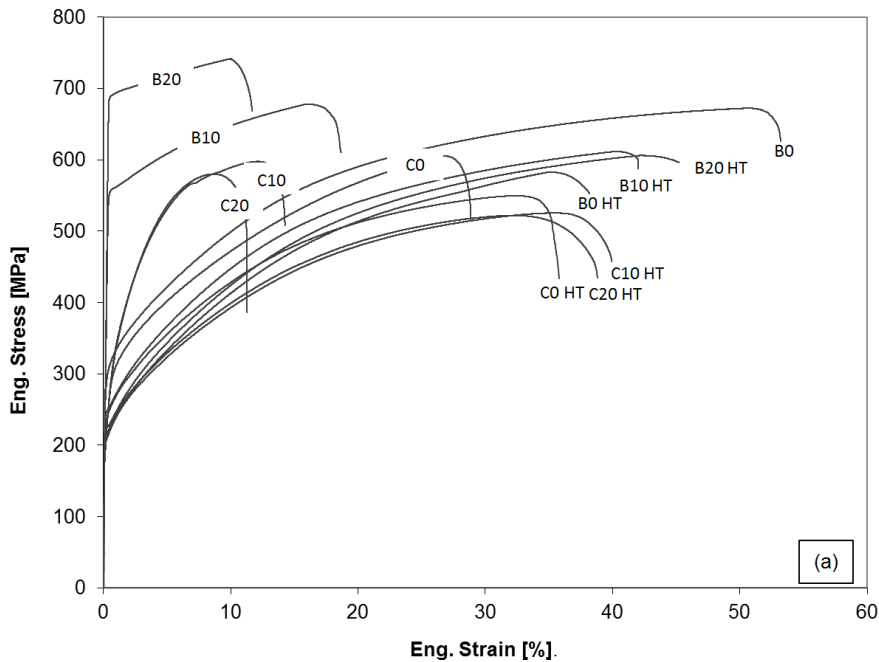
Fig. 4 (a) Global engineering stress-strain curves of all the specimens obtained by tension tests with the use of an extensometer; (b) Comparisons of strain values determined by DIC and extensometer (EXT) for plain specimens. 0.2% and 1% proof stresses determined from the curves are also tabulated.
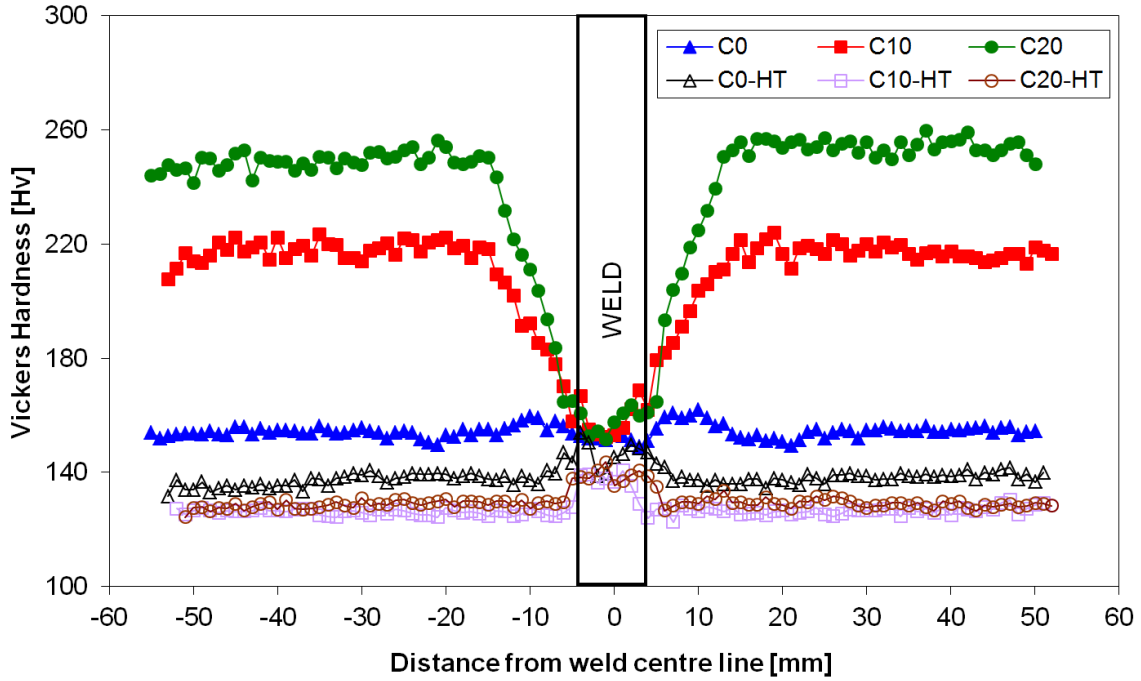
Fig. 5 Hardness profiles on the as-welded cross-weld specimens C0, C10 and C20 and heat-treated cross-weld specimens C0-HT, C10-HT and C20-HT.
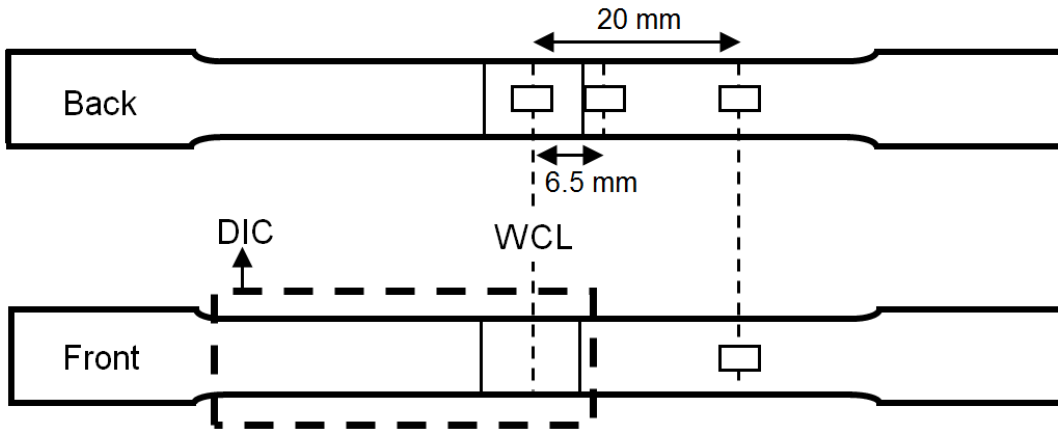
Fig. 6 Positions of strain gauges (SGs) on the back and front surfaces of cross-weld specimens.
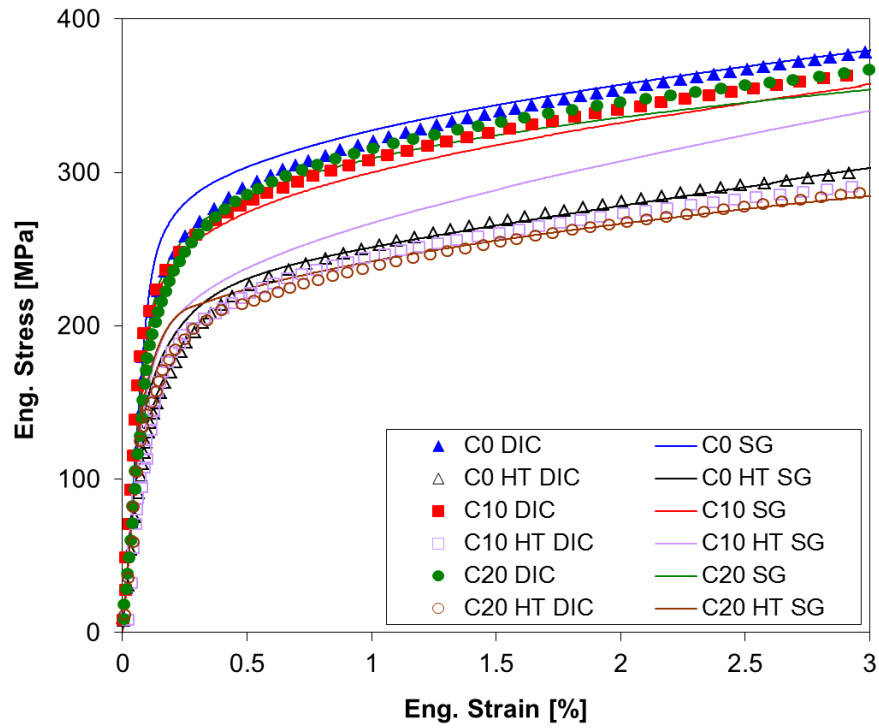
Fig. 7 Stress-strain data measured using strain gauges (SG) and DIC at the weld centre of cross-weld specimens.
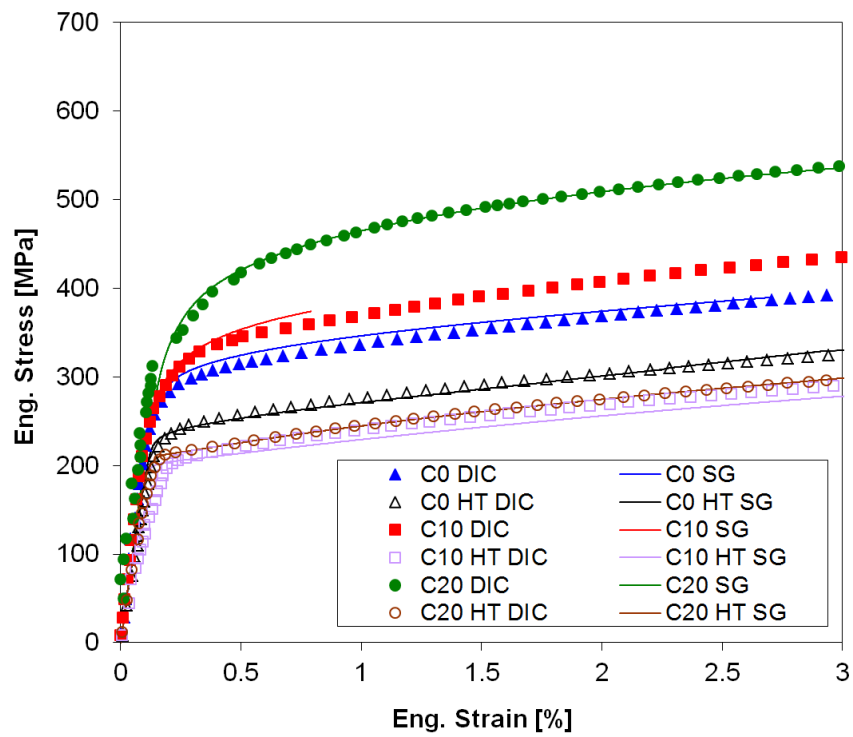
Fig. 8 Stress-strain data measured using strain gauge (SG) and DIC at 6.5mm from the WCL of cross-weld specimens.
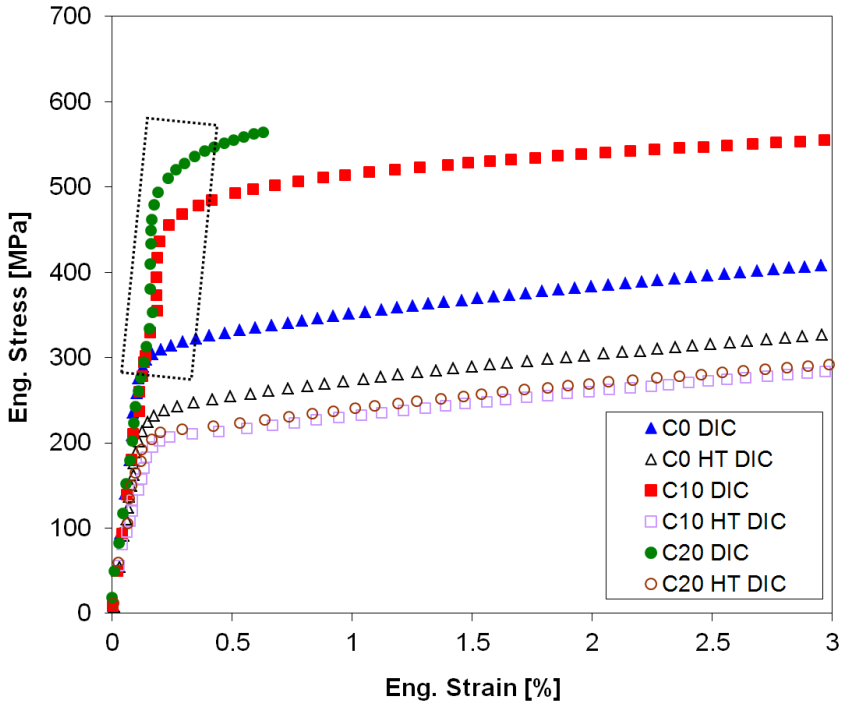
Fig. 9 Stress-strain data measured using DIC at 10mm from the WCL of cross-weld specimens.
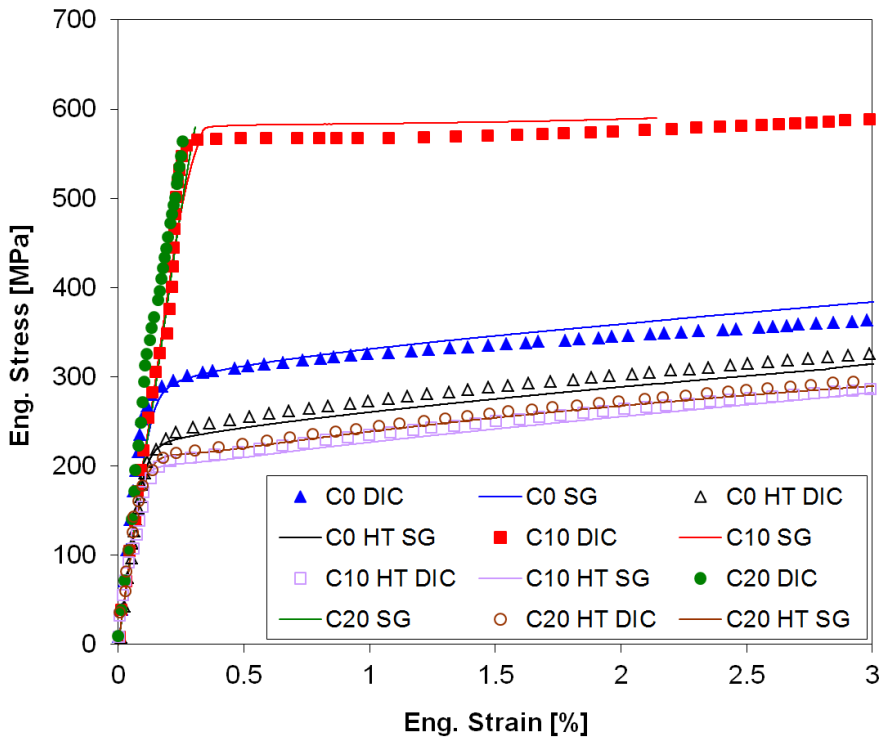
Fig. 10 Stress-strain data measured using SGs and DIC at 20mm from the WCL of cross-weld specimens.

Strain Gauges	0.2% Proof Stress (MPa)					
Position (mm)	C_0	C_{10}	C_{20}	$C_{0\text{-HT}}$	$C_{10\text{-HT}}$	$C_{20\text{-HT}}$
0 (back)	293	262	274	215	223	215
6.5 (back)	316	344	413	246	208	218
20 (back)	305	581	-	235	204	214
20 (front)	303	580	-	-	-	-
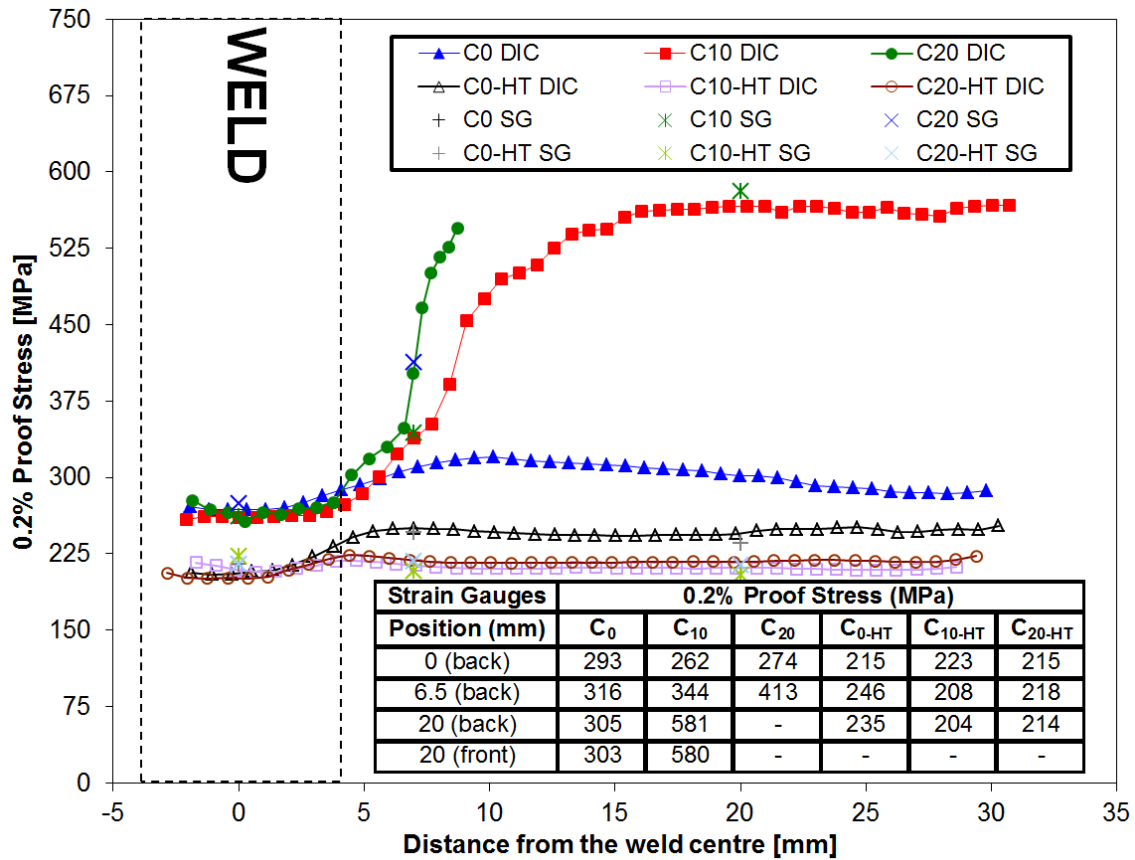
Fig. 11 Variation in 0.2% proof stress moving away from the WCL for cross-weld specimens (derived from SG and DIC data). Solid symbols represent the DIC data. Other symbols at WCL, 6.5mm and 20mm represent SG data. Open symbols are for the heat treated samples labelled with HT. 0.2% proof stress obtained from SG is also tabulated for different positions.
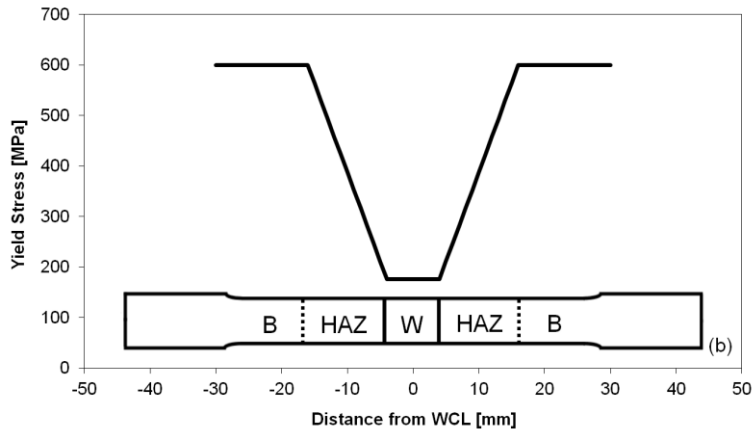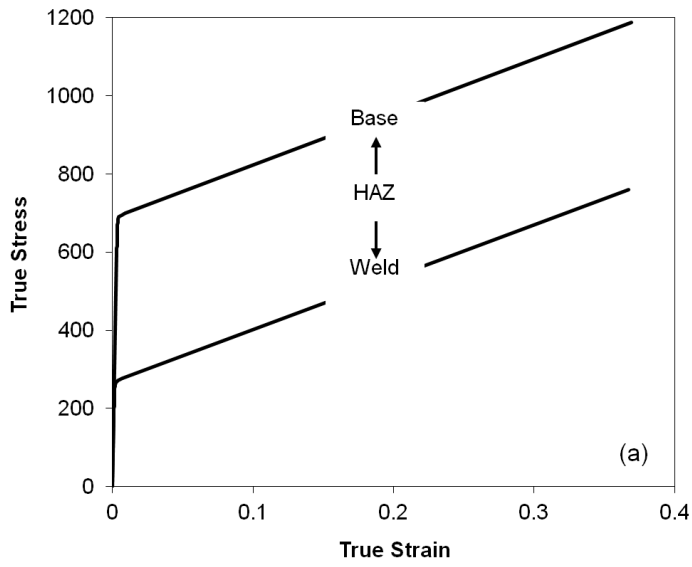
Fig. 12 Material properties input for FE model. (a) Input stress-strain curves (b) Input yield stress distribution along the specimen. Note that material properties in HAZ are continuous and there is no interface between unaffected base metal and HAZ.
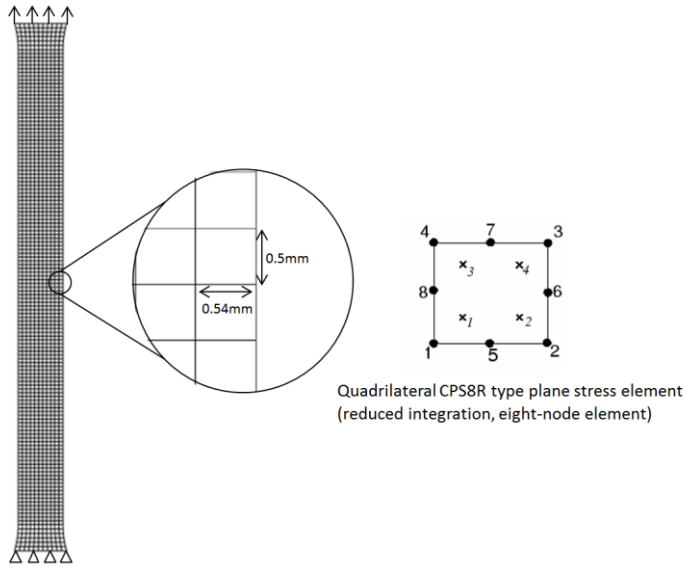
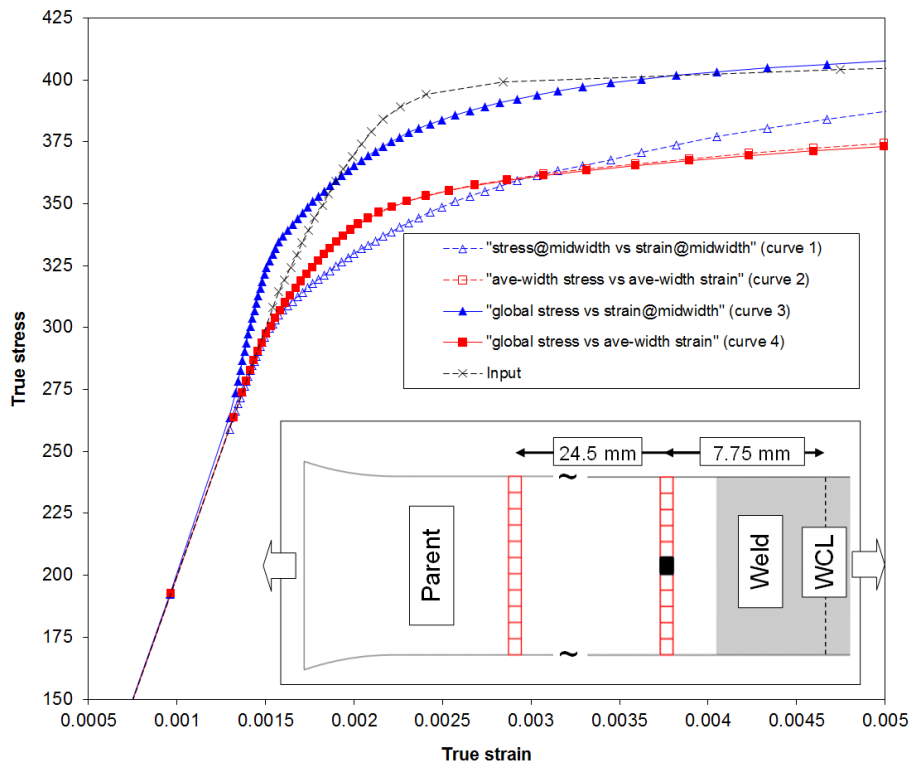Fig. 13 Finite element model mesh, element size and type

Fig. 14 The effect of iso-stress assumption (the use of global stress) on the stress-strain curves obtained from mid-width (filled domain) and averaged-width (unfilled & filled domains in a row) at 7.75mm away from WCL. Global stress was obtained from the average of axial stresses across the width (unfilled domains) at 24.5mm away from WCL.
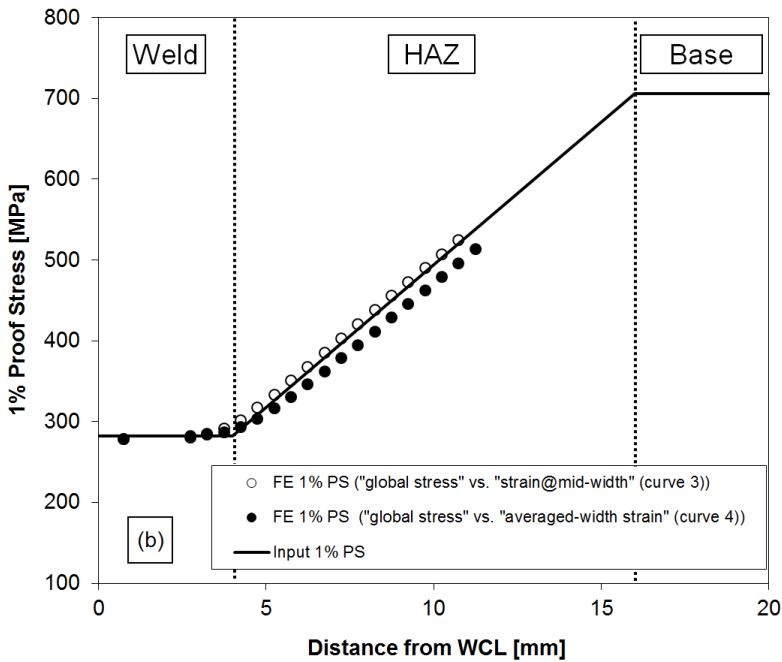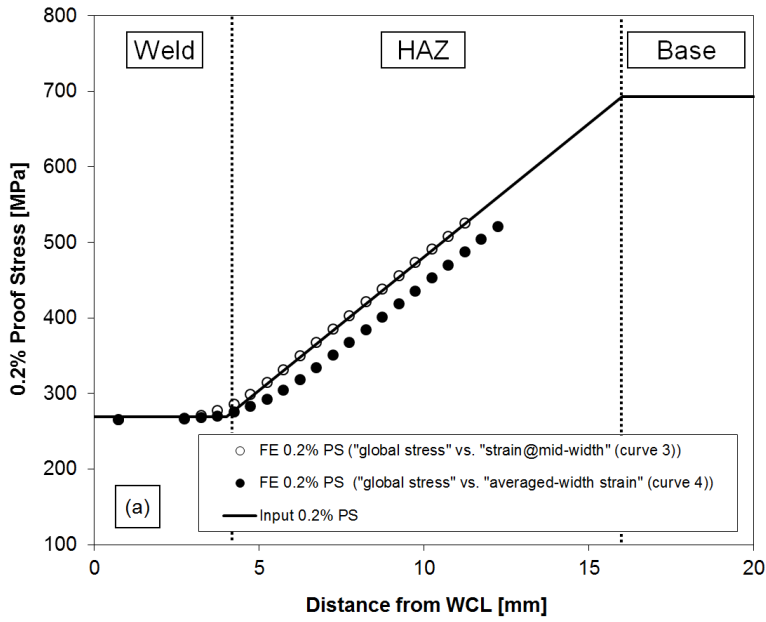
Fig. 15 Determination of 0.2% (a) and 1% (b) proof stress distribution along the half length of the specimen using curves (3) and (4) (see Fig. 14). Solid lines (—) correspond to the input 0.2% and 1% proof stress.
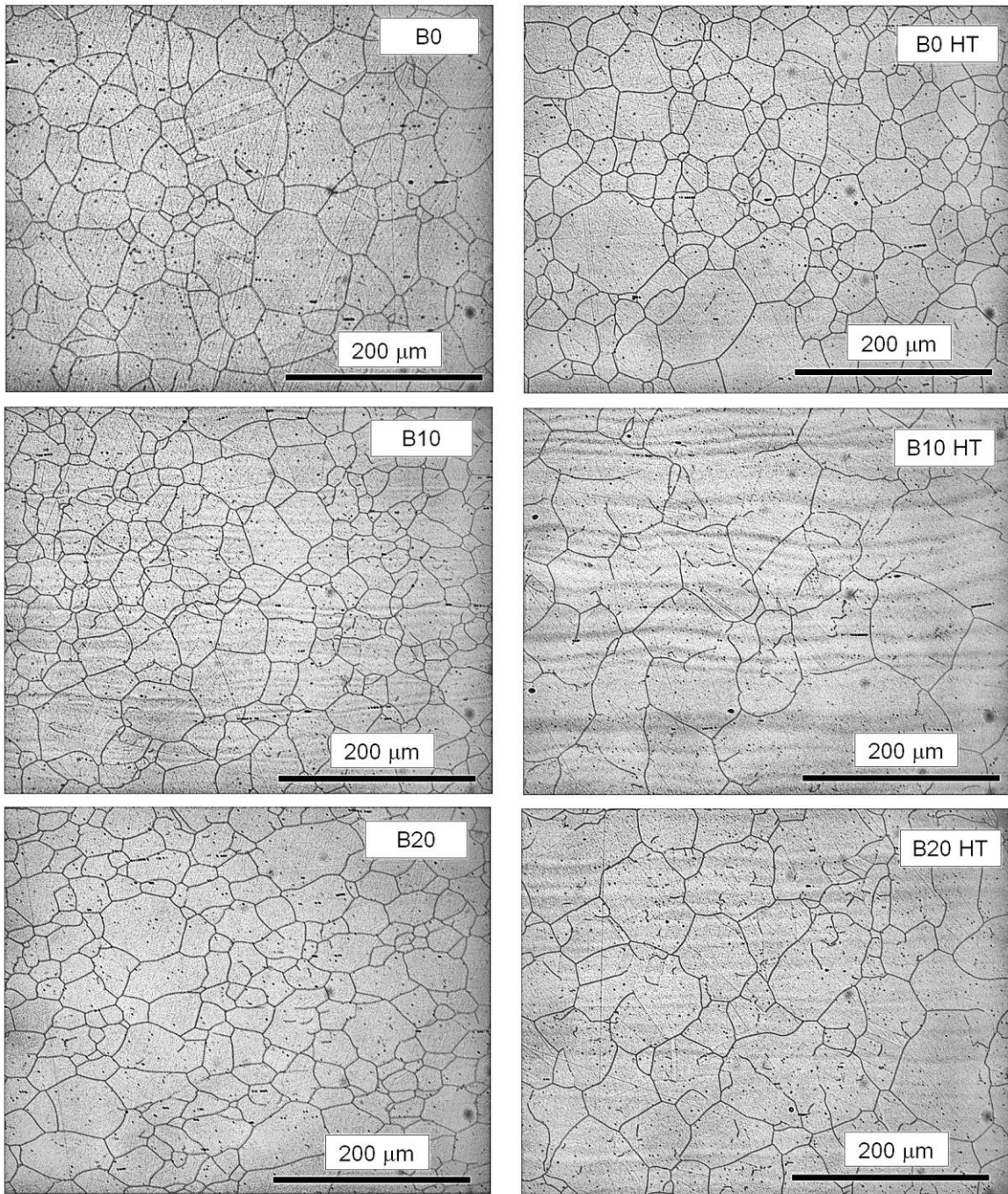
Fig. 16 The microstructures of the plain specimens before (B0, B10, B20) and after (B0-HT, B10-HT, B20-HT) the heat treatment on the RD-LD plane
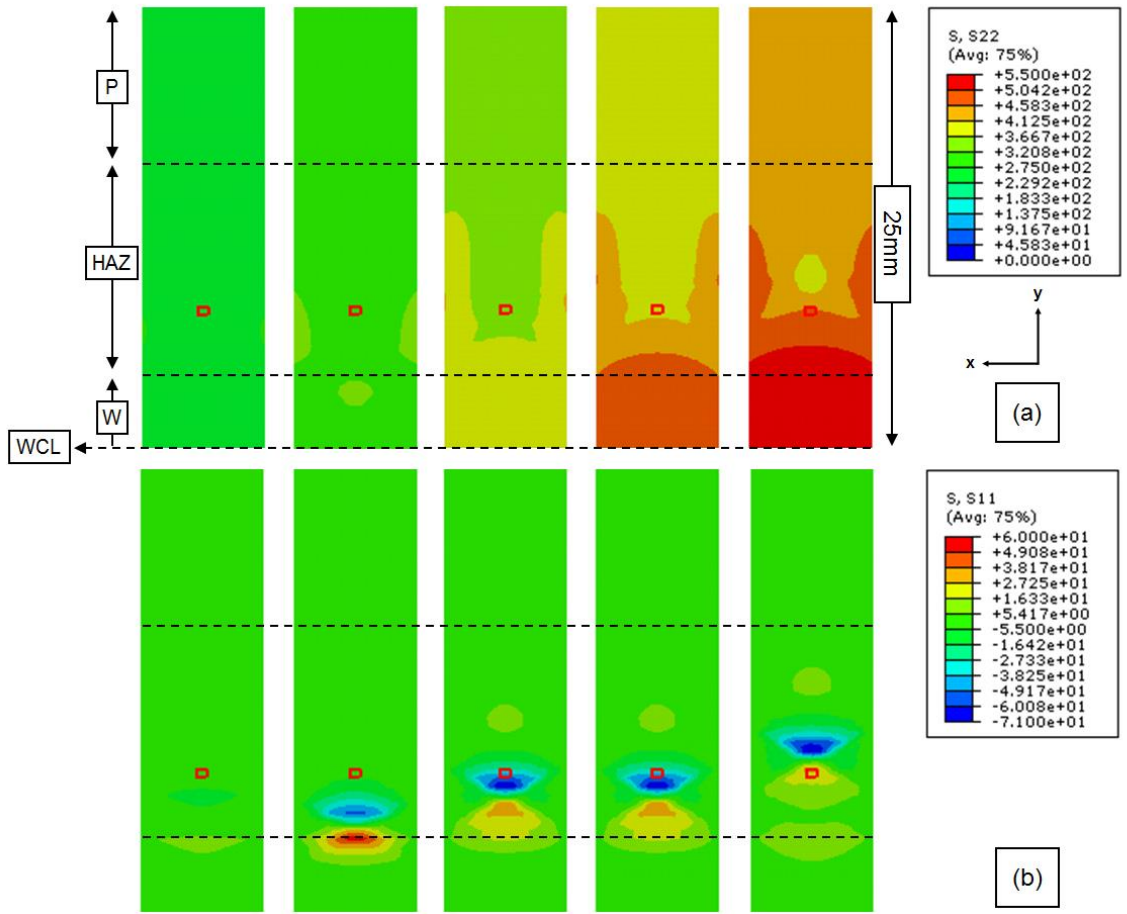
Fig. 17 Multi-material simulation results between WCL and 25mm away in the top half of the specimen at a global stress of 263, 304, 365, 407 and 440MPa (a) True stress (σ_{yy}) in loading direction (y-direction) (b) True stress (σ_{xx}) in the transverse direction (x-direction). The domain at the mid-width of 7.75mm is highlighted with a rectangle.